MID-IR PLASMON-MEDIATED PHOTOLUMINESCENCE FROM GALLIUM-DOPED ZINC OXIDE BOW-TIE NANOANTENNAS

BY

SUKRITH UMESH DEV

THESIS

Submitted in partial fulfillment of the requirements
for the degree of Master of Science in Electrical and Computer Engineering
in the Graduate College of the
University of Illinois at Urbana-Champaign, 2016

Urbana, Illinois

Adviser:

Associate Professor Daniel Wasserman

ABSTRACT

Semiconductor devices that interact with mid-infrared (mid-IR) wavelengths have a variety of applications in communications, sensing, and defense. However, most mid-IR sources, particularly incoherent emitters, are practically limited as a result of significant non-radiative losses. One proposed method of reducing these non-radiative losses is to use plasmonic materials due to their ability to enhance light-matter interactions. For inherently inefficient sources, such as many mid-IR emitters, coupling of the emitting element to a plasmonic structure could enhance emission efficiency.

This thesis explores the effectiveness of 3% gallium doped zinc oxide (GZO) as a mid-IR designer plasmonic material. We design, simulate, fabricate, and characterize a two-dimensional periodic array of bow-tie nanoantennas patterned on various mid-IR emitters. Thin films of GZO are grown by pulsed laser deposition and are characterized electrically and optically, with the extracted material parameters used as inputs in our simulations. GZO plasmonic nanoantennas are then fabricated. The spectral response of the patterned nanoantennas is then characterized using Fourier transform infrared reflection spectroscopy. Afterwards, samples are characterized by temperature and polarization dependent photoluminescence spectroscopy in order to determine the extent to which the emission efficiency improves as a result of coupling to the nanostructures.

To my family and Guru, for their love and wisdom.

ACKNOWLEDGMENTS

I acknowledge the incredibly large group of people who have helped me grow as a graduate student, especially my advisor, Professor Daniel Wasserman, and my fellow group members.

In addition, I acknowledge our collaborators at Wright Patterson Air-Force Base and Eglin Air Force Base as well as our collaborators at University of Massachusetts Lowell. Thank you all for your guidance and stimulating conversations.

And, of course, I thank my parents and sister for their constant encouragement.

TABLE OF CONTENTS

CHAPTER 1

INTRODUCTION

The mid-infrared (mid-IR) region of the electromagnetic spectrum has an abundance of applications, but also many challenges that often prevent the full and practical use of mid-IR devices. Many molecules have vibrational bands in the mid-IR [1], which naturally makes mid-IR emitters and detectors especially useful in spectroscopy, sensing and defense. In addition, there are two prominent atmospheric transparency bands in the mid-IR, the 3-5 μm and 8-12 μm wavelength bands, which could have potential applications in free space optical communication systems [2].

However, many mid-IR, narrow-bandgap semiconductors experience difficulties when operating at practical temperatures [3]. Detectors, for example, require cooling as they are affected by thermal noise and therefore have very poor signal-to-noise ratios at room temperature. While there is much research being done on mid-IR detectors [4], this thesis primarily explores one possible solution to some practical problems associated with mid-IR emitters.

The primary objective of an emitter is obviously to emit light. However, most mid-IR emitters are limited by non-radiative losses such as Shockley-Read-Hall (SRH), phonon-assisted scattering, and Auger recombination [3], which prevent them from achieving practical efficiencies at higher temperatures. Plasmonic materials may provide a solution.

In general, plasmonic materials, despite their many interesting phenomena such as subwavelength confinement [5] or extraordinary transmission [6], have received much criticism for being impractical mainly due to scattering and absorption losses in the metal. However, since mid-IR emitters already experience significant non-radiative losses, coupling the emitter to a plasmonic material could, in fact, provide an overall increase in emission, especially at higher temperatures. Of course, for this to work, metallic losses in the plasmonic material must be lower than non-radiative losses in the emitter.

The remainder of this thesis initially evaluates the effectiveness of 3%

gallium-doped zinc oxide (GZO) as a plasmonic material in the mid-infrared by obtaining key parameters such as plasma frequency and scattering using Fourier transform infrared (FTIR) reflection spectroscopy and transfer-matrix method (TMM) fitting. Then, results from simulation, fabrication, and characterization of 2D periodic GZO bow-tie nanoantennas are shown followed by a discussion and analysis.

CHAPTER 2

CHARACTERIZATION OF GZO AS A MID-IR PLASMONIC MATERIAL

In this chapter, a brief overview of the Drude model and the transfer-matrix method (TMM) is provided. Then, using reflection spectroscopy, a spectrum of a thin (293 nm determined by collaborators using ellipsometry) layer of GZO is obtained and then fitted to a calculated spectrum using the TMM; this allows for the plasma frequency, ω_p, and the mean free scattering, γ, to be extracted.

2.1 The Drude Model

Using Newton's second law, it is possible to write all of the forces on a free particle [7]:

$$m\frac{dx^2}{dt^2} + m_0\gamma\,\frac{dx}{dt} = -eE \tag{2.1}$$

The first term, often called the inertial term, is simply the mass times the acceleration of a free particle. The second term, which may be neglected in the case of a cold, collisionless plasma, refers to the scattering of the particle. Finally, the term on the right-hand side of equation 2.1 is the force on a charge due to an electric field [7]. Clearly, this is a differential equation that can be solved for the position in terms of the electric field:

$$x(t) = \frac{e}{m(\omega^2 + i\gamma\omega)}E(t) \tag{2.2}$$

Then, considering the relationship between displaced electrons and macroscopic polarization, $\mathrm{P} = -nex(t)$, and $\mathrm{D} = \epsilon\mathrm{E}$, the permittivity is derived to be

$$\epsilon(\omega) = 1 - \frac{\omega_p^2}{\omega^2 + i\gamma\omega} \tag{2.3}$$

with $\omega_p^2 = \frac{ne^2}{\epsilon_0 m^*}$. When considering background dielectrics other than air, the additional contributions from the bound charges are included [5], so we redefine $\omega_p^2 = \frac{ne^2}{\epsilon_0 \epsilon_b m^*}$, and:

$$\epsilon(\omega) = \epsilon_b - \frac{\omega_p^2}{\omega^2 + i\gamma\omega} \tag{2.4}$$

Before simulating and fabricating the nanoantennas made with GZO, it was necessary to first obtain the plasma frequency and scattering. To do this, a thin layer of GZO was grown on a silicon wafer by collaborators at Wright-Patterson Air Force Base (WPAFB) using pulsed laser deposition. Once grown, reflection spectroscopy using our FTIR was used to obtain an experimental spectrum. From here, using a transfer matrix method (TMM), we calculated the reflection spectrum experimentally and used a Drude model to model the layer of GZO. When the correct values for ω_p and γ are used, the spectra calculated using TMM and the experimentally determined spectrum would match.

2.2 Fresnel Reflection and Transmission Coefficients

Before considering the total reflection from multi-layered slabs, it is first necessary to determine the reflection and transmission coefficients from a single interface, shown in figure 2.1. For a transverse electric field (TE) mode, from Maxwell's first boundary condition (tangential electric field continuity) and phase matching, Snell's law relating the incident, reflected, and transmitted light is derived [7]:

$$\theta_i = \theta_r \tag{2.5}$$

$$n_1 sin\theta_i = n_2 sin\theta_t \tag{2.6}$$

Assuming non-magnetic material, the expression for the index of the refraction is simply the square root of the permittivity: $n = \sqrt{\epsilon}$. Then, by utilizing the continuity of the tangential magnetic fields, expressions for the reflection and transmission coefficient of TE mode are:

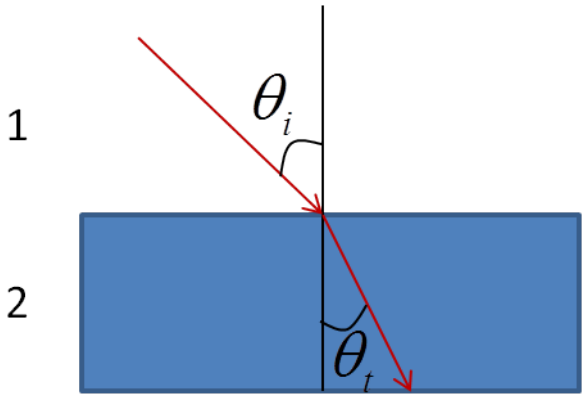

Figure 2.1: Light incident on an interface at an oblique angle, θ_i, and transmitted at angle θ_t.

$$r_{TE} = \frac{n_1 cos\theta_i - n_2 cos\theta_t}{n_1 cos\theta_i + n_2 cos\theta_t} \tag{2.7}$$

$$t_{TE} = 1 + r_{TE} = \frac{2n_1 cos\theta_i}{n_1 cos\theta_i + n_2 cos\theta_t} \tag{2.8}$$

For the case of a transverse magnetic field, a similar procedure can be done to obtain:

$$r_{TM} = \frac{n_1 cos\theta_t - n_2 cos\theta_i}{n_1 cos\theta_t + n_2 cos\theta_i} \tag{2.9}$$

$$t_{TM} = 1 + r_{TM} = \frac{2n_1 cos\theta_t}{n_1 cos\theta_t + n_2 cos\theta_i} \tag{2.10}$$

At normal incidence, the reflection and transmission coefficients are equal in both the TE and TM case and are simplified to be [7]:

$$r = \frac{n_1 - n_2}{n_1 + n_2} \tag{2.11}$$

$$t = 1 + r = \frac{2n_1}{n_1 + n_2} \tag{2.12}$$

2.3 The Transfer Matrix Method

In the previous section, the Fresnel reflection coefficients across a single interface were derived. However, in order to extract the plasma frequency and

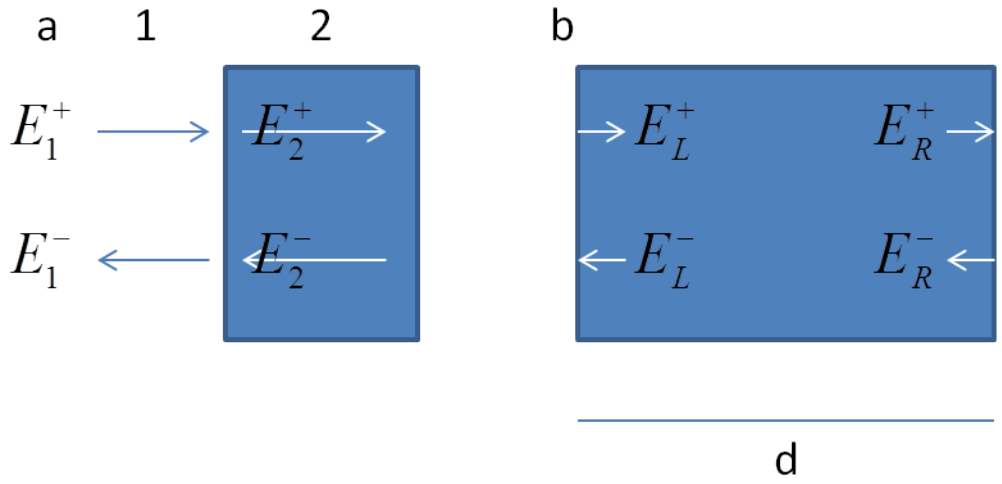

Figure 2.2: Field definitions for (a) an interface change, and (b) propagation in a medium of thickness d.

scattering from experimental reflection data, multiple layers must be considered as the GZO is grown on a substrate. Using the matrix optics approach described by [7] and [8], it is clear that to describe the overall reflection of a multilayer system, a product of interface reflection and medium propagation matrices must be obtained. This product matrix, often called the backwards propagation matrix, relates the entering and exiting fields from the top of the layer stack to the fields entering and exiting the bottom of the layer stack. Figure 2.2 shows the field definitions for the case of an interface change and propagation through a medium of thickness d. A matrix T_{12} relating the fields on one side of the interface to the other side (from material two to material two) is used to describe the change in fields every time there is a a new layer:

$$\begin{bmatrix} E_1^+ \\ E_1^- \end{bmatrix} = T_{12} \begin{bmatrix} E_2^+ \\ E_2^- \end{bmatrix} = \begin{bmatrix} \frac{1}{t_{12}} & \frac{r_{12}}{t_{12}} \\ \frac{r_{12}}{t_{12}} & \frac{1}{t_{12}} \end{bmatrix} \begin{bmatrix} E_2^+ \\ E_2^- \end{bmatrix}$$

In the expression above, r_{12} and t_{12} are the Fresnel reflection and transmission coefficients, respectively, when a field in medium one is incident on medium two. After every layer/interface change, the field then propagates through the medium's thickness, d. As it does this, the phase of the field changes based on how far it propagates through the medium as well as the index of refraction of the medium. At normal incidence, this phase shift

matrix, which relates the fields of the free-space wavelength, λ_0, at the beginning of the layer and toward the end of the layer with refractive index n, is given by:

$$\begin{bmatrix} E_L^+ \\ E_L^- \end{bmatrix} = P \begin{bmatrix} E_R^+ \\ E_R^- \end{bmatrix} = \begin{bmatrix} e^{-i\frac{2n\pi}{\lambda_0}d} & 0 \\ 0 & e^{i\frac{2n\pi}{\lambda_0}d} \end{bmatrix} \begin{bmatrix} E_R^+ \\ E_R^- \end{bmatrix}$$

Hence, to describe a system with n layers, and no incident wave from the bottom of the stack, a total transfer matrix, S, can be derived by multiplying the interface change matrix with the propagation matrix for each layer:

$$\begin{bmatrix} E_0 \\ rE_0 \end{bmatrix} = T_{12} \times P_2 \times T_{23} \times P_3 \times ... \times P_{n-1} \times T_{n-1,n} \times \begin{bmatrix} tE_0 \\ 0 \end{bmatrix}$$

$$= S \begin{bmatrix} tE_0 \\ 0 \end{bmatrix} = \begin{bmatrix} S_{11} & S_{12} \\ S_{21} & S_{22} \end{bmatrix} \begin{bmatrix} tE_0 \\ 0 \end{bmatrix}$$

The overall reflection of the multilayer system is then described by:

$$r = \frac{S_{21}}{S_{11}} \tag{2.13}$$

Using the TMM method, a theoretical reflection spectrum can be calculated. By varying the plasma frequency and scattering of the GZO, the calculated spectrum is changed until it sufficiently matches the experimentally determined reflection spectrum using FTIR.

2.4 Results from GZO Material Characterization

2.4.1 Initial GZO Thin Film Characterization

Using the TMM and FTIR reflection spectroscopy, we characterized the initial GZO sent to us. Using ellipsometry, the initial GZO layer was determined by our collaborators at WPAFB to be 293 nm thick. In figure 2.3, the experimental and calculated spectra are shown.

Clearly, there is a reasonable match between the calculated and experimental spectra. For this initial GZO thin-film, we extracted a plasma wavelength $\lambda_p = 1.29$ μm (corresponding to plasma frequency $\omega_p = 1.46 \times 10^{15}$ rad/sec) and a scattering $\gamma = 5.5 \times 10^{14}$ s^{-1}.

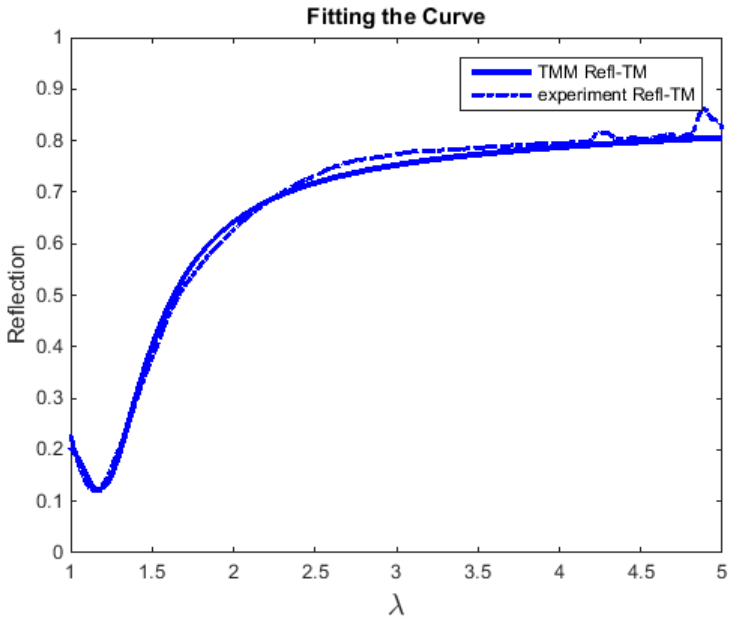

Figure 2.3: There is a reasonable fit between the experimental and calculated reflection spectra when $\lambda_p \approx 1.29$ μm and $\gamma \approx 5.5 \times 10^{14}$ s^{-1}

2.4.2 Issues with the Initial GZO

With a scattering term of 5.5×10^{14} s^{-1}, the losses in the initial thin-film were too high; after discussion, it was thought that either that particular deposition of GZO was lossy, or there were problems associated with the reflection measurements and fitting. For this reason, our collaborators at WPAFB used their Hall-effect system to extract mobility, μ, and carrier concentration, N, from the GZO; these values were then converted to a plasma frequency and a scattering term using

$$\omega_p^2 = \frac{Ne^2}{m^*\epsilon} \tag{2.14}$$

and

$$\gamma = \frac{e}{\mu m^*} \tag{2.15}$$

After a few different depositions of GZO, the highest mobility (least lossy) value that was consistently obtained was $\mu = 24$ cm^2/Vs, which corresponded to a scattering term of approximately $\gamma = 2 \times 10^{14}$ s^{-1}, which is at least two and half times less lossy than the initial film. From the Hall-Effect data, our collaborators reported a carrier concentration of approximately

$N = 9.52 \times 10^{20}$ cm^{-3}, which corresponds to a plasma wavelength of $\lambda_p = 1.29$ μm; this value is consistent with the TMM extracted plasma wavelength. With these later films, since the plasma wavelength is similar to that of the initial film, but the losses are significantly less, we were satisfied with the overall quality of the GZO as a mid-IR plasmonic material and therefore proceeded to simulate GZO bow-tie nanoantennas.

CHAPTER 3

SIMULATIONS OF GZO BOW-TIE NANOANTENNAS

In this chapter, we use a rigorous coupled wave analysis (RCWA) code written by our collaborators in V. Podolskiy's group at the University of Massachusetts Lowell in order to simulate both the far-field and near-field spectral response of 2D periodic GZO bow-tie nanoantennas patterned on top of our emitter. For these simulations, we assumed the emitter was indium arsenide (InAs), but our actual emitter material is discussed in chapter 4.

3.1 The Bow-Tie Nanoantenna Geometry

When searching for a plasmonic resonance with our simulations, our goal was to correlate reflection peaks at a certain wavelengths with strong near fields in the gap of the bow-tie nanoantenna. From simulations, we determined that the bow-tie gap affected the near-field strength the most but did not affect the far-field reflection spectrum. Ultimately, the plasmonic far-field reflection peak was affected by the material parameters of the GZO as well as the periodicity and fill-factor of the bow-tie; this is not very surprising, as these parameters affect the ability to couple to plasmons using a grating [9]. In figure 3.1, an overhead view of the geometry for a single square of the 2D periodic array is shown.

3.1.1 Simulations Using the Initial GZO Film

For the first set of simulations, we used the initial GZO film that was later deemed too lossy for mid-IR applications. From the simulations, the far field reflection spectrum lacks any mid-IR reflection peaks indicative of coupling to plasmons; when plotting the near-field, however, we do see a near-field enhancement. Figure 3.2 shows the TM far-field reflection spectra and figure

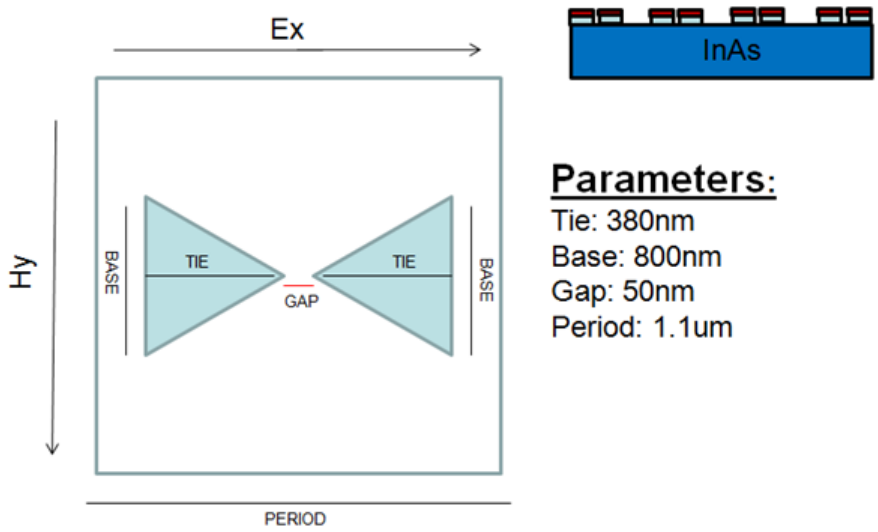

Figure 3.1: Overhead view of the bow-tie geometry. The GZO thickness varied per sample, and the silicon dioxide is approximately the result of exposed and developed HSQ e-beam resist, discussed in chapter 4. Electric and magnetic field directions are shown.

3.3 shows both the overhead XY cross section and the XZ cross section TM E-field enhancements.

The field enhancement is thought by [5] to be a combination of enhancement from the geometry (lightning rod effect) and material (plasmonic resonance). Since this initial GZO film is very lossy, it is the logical conclusion that the near field enhancement seen in figure 3.3 is likely a result of the lightning rod effect from the sharp edges of the bow-tie and nanometer-scale bow-tie gap size. From the earlier TMM fit, we thought that this initial GZO was too lossy; after completing simulations, it was without doubt that for a practical device, less lossy GZO would be required.

3.1.2 Simulations Using a Lower-Loss GZO Film

Once higher quality (larger mobility and less lossy) thin-film GZO was developed, simulations were done again with the same bow-tie geometry but using the less lossy GZO as the plasmonic bow-tie material. This time, on the far-field reflection spectra, a reflection peak is present at approximately $\lambda \approx 4.0\ \mu$m. In addition, the near-field enhancement is much greater than it was with the initial, lossier film. Figure 3.4 shows the far-field spectrum,

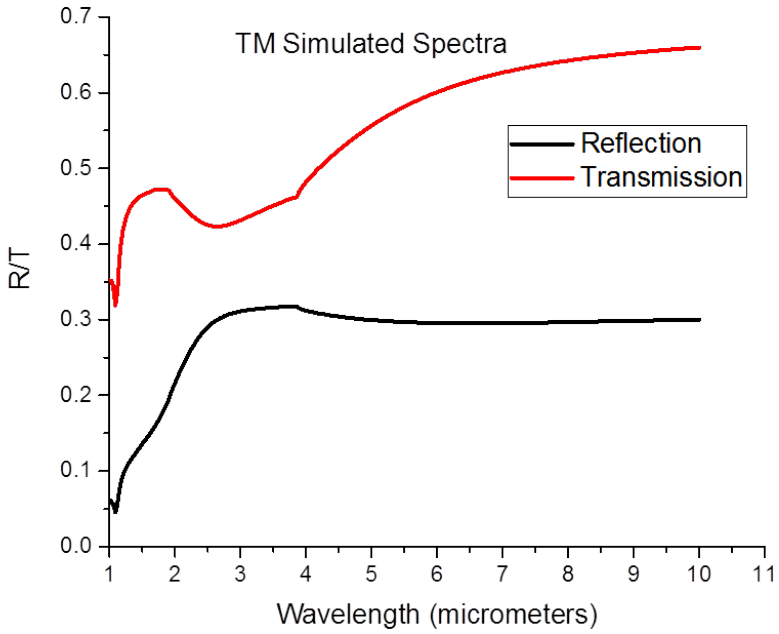

Figure 3.2: Far-field spectrum for the initial GZO film bow-tie nanoantennas calculated using RCWA.

and figure 3.5 shows the TM fields for the XY and XZ cross sections at the maximum enhancement wavelength.

From these low-loss GZO bow-tie nanoantenna simulations, since there is a spectral overlap between the TM polarized far-field reflection peak and the near-field enhancement, it was decided that fabrication is the next step.

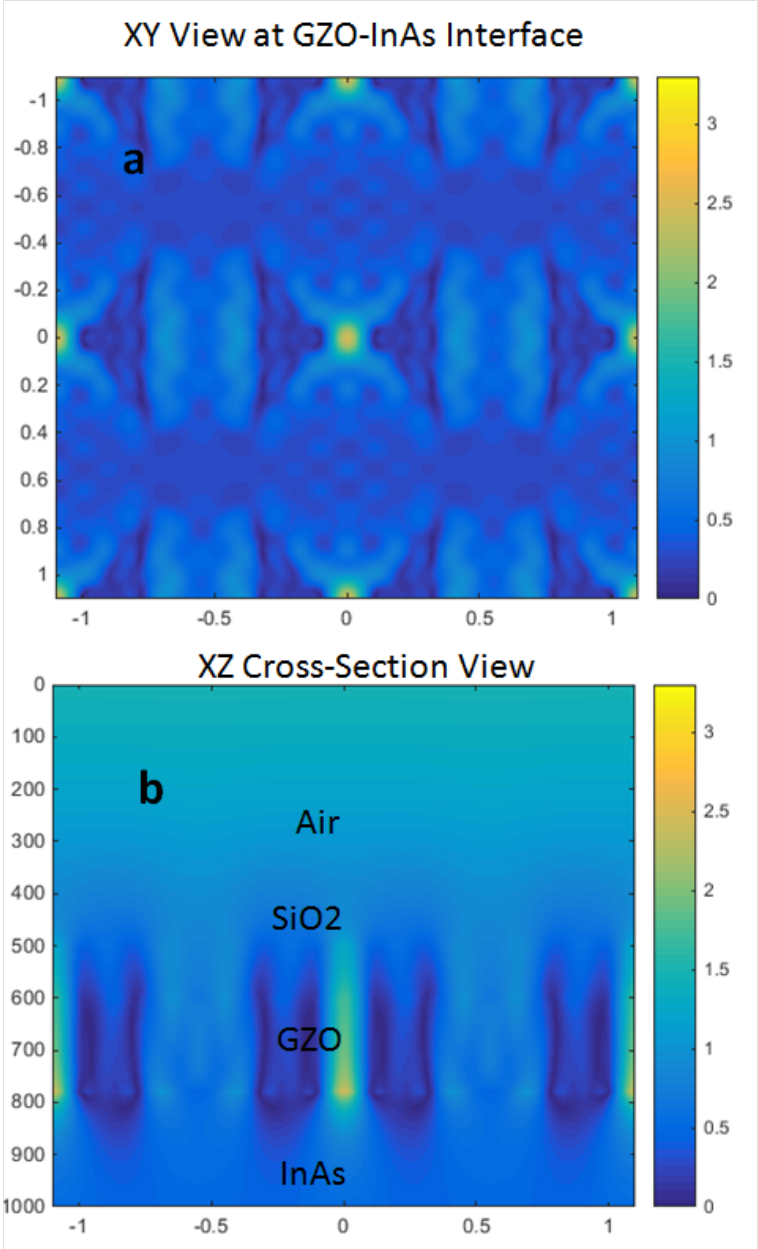

Figure 3.3: TM E-field magnitude for the nanoantennas fabricated with the initial GZO film at $\lambda \approx 3.8$ μm in (a) XY overhead view at the GZO-InAs interface, and (b) XZ cross-section view.

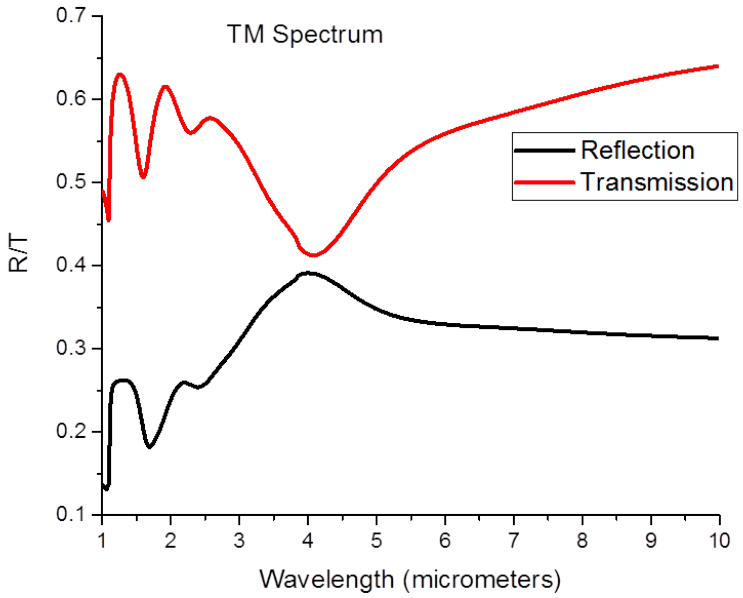

Figure 3.4: Far-field spectrum for the lower-loss GZO film bow-tie nanoantennas calculated using RCWA.

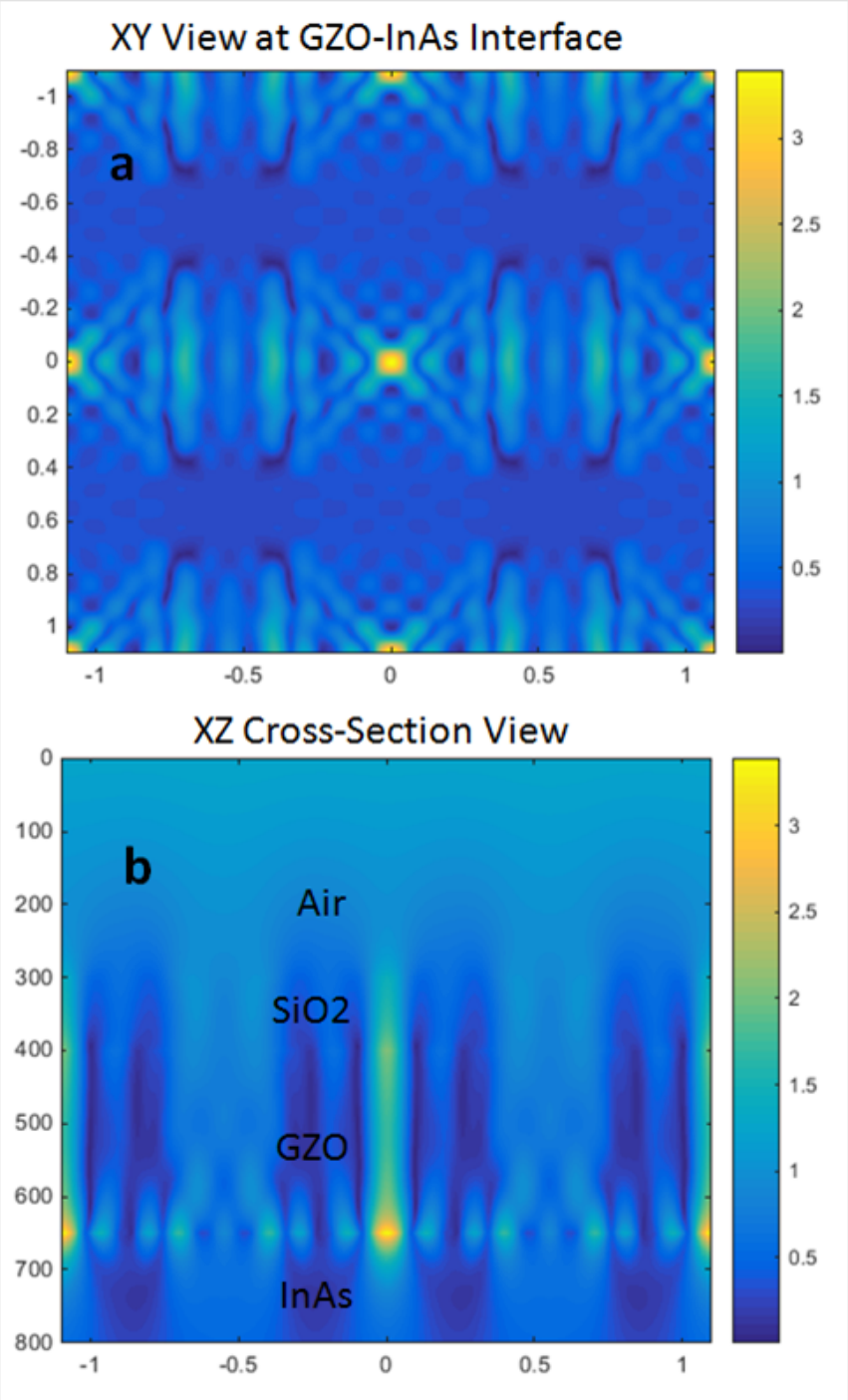

Figure 3.5: TM E-field magnitude at $\lambda \approx 4.2$ μm in (a) XY overhead view at the GZO-InAs interface, and (b) XZ cross-section view.

CHAPTER 4

FABRICATION OF GZO BOW-TIE NANOANTENNAS

In this chapter, the fabrication of the GZO bow-tie nanoantennas is discussed in detail. The nanoantennas thus far have been grown on three different emitters, with SEM images provided for the initial two sets. All photoluminescence and reflection data is shown in chapter 6.

4.1 Initial Fabrication of Bow-Ties On Indium Arsenide

In previous chapters, it was claimed that the initial GZO film was too lossy; however, since this was what we had at the time, we attempted to fabricate the nanoantennas with this material anyway to serve as a practice fabrication at the very least. For the emitter material, we just used a piece of an undoped indium arsenide (InAs) wafer purchased from WaferTech LLC.

4.1.1 Deposition of GZO

The deposition of GZO was done using pulsed laser deposition by our collaborators at WPAFB using a 3% gallium oxide containing zinc oxide target [10]. Using ellipsometry, a thickness of approximately 180 nm was determined. For this film, as mentioned earlier, a plasma wavelength $\lambda \approx 1.29$ μm and scattering $\gamma = 5.5 \times 10^{14}$ s^{-1} were obtained using a TMM fit.

4.1.2 Patterning Using Electron-Beam Lithography

Because of the small bow-tie gap size feature (50 nm) necessary to obtain strong near-field enhancements, electron-beam lithography (EBL) was nec-

essary to pattern the deposited GZO layer. The EBL was performed using the WPAFB clean room with help from collaborators.

Since we will eventually need to perform photoluminescence experiments (explained in chapter 5) on the bow-tie nanoantenna array for testing purposes, it was clear that we would need at least a 50 μm $\times$ 50 μm square array of bow-ties per pattern to account for the exciting lasers beam spot size. However, since each bow-tie has a period in each direction of 1.1 μm, patterning the 2500 μm^2 would involve the EBL machine to write nearly 2500 bow-ties per pattern. Hence, since the writing time could potentially be a concern, we decided to use a negative e-beam resist (EBR) so that the machine would need to only write the areas where bow-ties would be present rather than write areas across the entire sample that did not have bow-ties.

Since we were searching for a high-resolution, negative EBR, hydrogen silsesquioxane (HSQ) was the logical choice. Initially, we were not certain what gap size resolution we could achieve; for this reason, we created four different pattern sets using the bow-tie dimensions simulated earlier, but with gap sizes varying from 40 nm to 100 nm in 20 nm increments.

The thickness of the HSQ is controllable by either diluting the HSQ with MIBK or by spinning the resist with less rpm. However, if the rpm is too low, the EBR may not be uniform across the sample when spun. Hence, diluting the EBR to obtain the desired thickness was the better option. Since the GZO layer is 180 nm, we estimated that our HSQ should ideally be less than 120 nm in thickness. Hence, we decided to dilute the 6% HSQ we had to 4% so that when spun at a high speed (4000 rpm for 40 s), the sample would be uniformly covered in slightly less than 120 nm of HSQ EBR. Once spun, the sample would be baked at 100 °C for approximately 5 minutes. For exposure, we tried dosages of both 500 μC/cm^2 and 1000 μC/cm^2; ultimately, there was no noticeable difference between the two dosages. After exposing, the sample was developed using AZ300MF (2.38% TMAH solution) developer for 70 s [11].

After development, the HSQ is known to form an oxide very close to silicon dioxide. Generally, the silicon dioxide could be etched off using a BOE or HF solution, but since this risks etching the GZO, this was not an option; despite this, since the coupling from the emitter to the nanoantennas depends on the InAs-GZO interface, leaving the silicon dioxide on top of the GZO after etching should not affect the performance of the enhanced emitter.

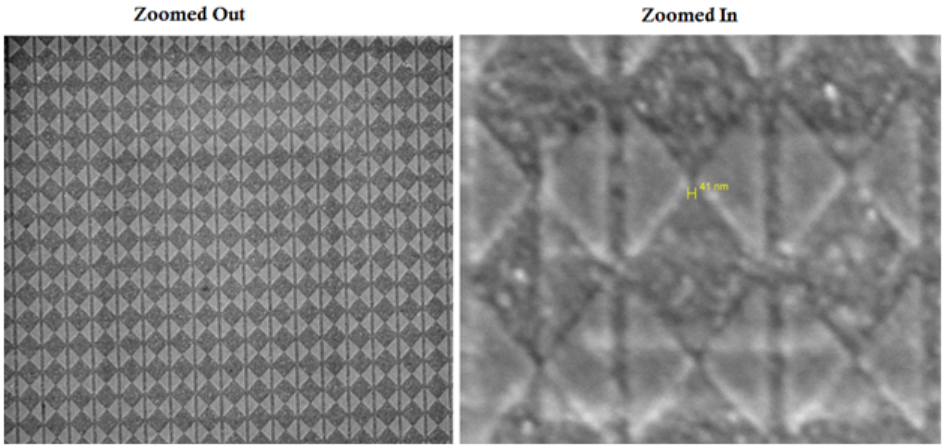

Figure 4.1: Overhead SEM view of the initial set of bow-ties which shows that the e-beam process achieved the desired resolution. However, nothing can be said about the extent of undercutting from the etch.

4.1.3 Etching

With this initial set of bow-ties, since dry-etching machines (RIE, ICP-RIE) were unavailable at the time, we considered using wet etching the GZO using a slightly acidic (pH 5) HCl and DI water solution. While undercutting is a serious issue with wet etching, especially when we are attempting to achieve 50 nm bow-tie gap sizes, we were anyway going to fabricate another set of bow-ties on another emitter material. Also, we considered the possibility that the undercutting would not affect the InAs-GZO interface too much. In figure 4.1, we show overhead SEM images of the 40 nm gap bow-ties; from the SEM, we were able to determine that our e-beam lithography is able to achieve a resolution of at least 40 nm. However, from an overhead view, the top layer is the silicon dioxide e-beam mask; hence, we cannot determine the extent of undercutting the GZO experienced from a wet etch. From the experimental results (discussed in later chapters), this set of nanoantennas did not work. Since the undercutting from the wet etch was one of the most likely reasons, we used dry etching for future samples.

4.1.4 Creating Gold Windows

The thickness of a human hair is on the order of hundreds of microns. Each pattern of bow-tie nanoantennas, however, is 2500 μm^2 in size. Because of

difficulties in being able to aim a laser precisely at the pattern, we created gold windows around the patterns using standard contact lithography. In addition, we created an extra window without any nanoantennas to serve as a control sample as a means of ensuring that the same area of emitter material is excited in windows with and without nanoantennas.

For this process, standard AZ5214 photoresist (PR) was spun on. After a 110 °C bake and edge bead removal, the windows were exposed. Next, the sample was baked at 160 °C with high-humidity to serve as the reversal bake. Finally, the sample was flood exposed for 70 s. The sample was developed using a 5:1 DI water:AZ351MF developer solution for 30 s.

Once developed, the sample was put into a metal evaporator. First, a thin (3 nm) titanium adhesion layer was evaporated followed by a 30 nm layer of gold. After evaporation, a simple acetone liftoff was used to lift windows where there were bow-ties on the control sample. The device was now completely fabricated and ready for testing.

4.2 Fabrication of Bow-Ties on $\lambda \approx 3.8$ μm Mid-IR Emitters

The last section describes the overall fabrication process for these bow-tie nanoantennas. However, since it was a first attempt, the emitter we used was just a piece of plain InAs, which emits at $\lambda \approx 3$ μm at 77 K. However, since we are originally aiming for emission around $\lambda \approx 4$ μm, we used an emitter from a previous project with an epsilon-near-zero (ENZ) layer which emitted at $\lambda \approx 3.8$ μm.

4.2.1 Differences in the Process

For the most part, the process was the same as mentioned before. However, we attempted to correct mistakes made in the previous batch of nanoantennas. First, we were able to deposit a GZO film that was significantly less lossy than the initial film (discussed in earlier chapters), and the film was grown on a $\lambda \approx 3.8$ μm mid-IR emitter rather than InAs. Results from ellipsometry revealed a thickness of approximately 232 nm.

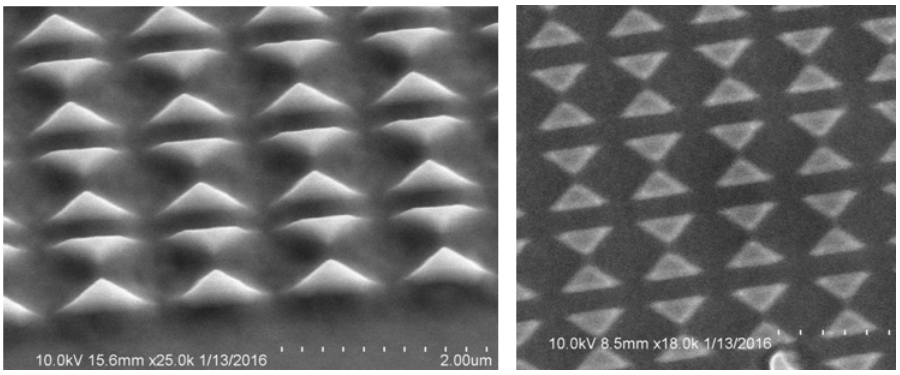

Figure 4.2: Angled SEM view (left) and overhead SEM view (right) of the new set of bow-tie nanoantennas.

Once the GZO was deposited, since we were content with the results from the EBL from the previous batch, we did not change anything significant in the EBL patterning stage except for the size of the nanoantenna areas; this time, for additional ease of testing, each 2D array of bow-ties was repeated in an area of 220 μm $\times$ 220 μm instead of 50 μm $\times$ 50 μm like before. Also, because of inevitable underetching using a wet-etch, we decided to use an inductive coupled plasma reactive ion etch (ICP-RIE) machine to dry etch the pattern and obtain a much more anisotropic etch.

While many report etch rates for ZnO such as [12] and [13], we decided to use [14] as this seemed to be the fastest etch rate. For this dry etch, the key gas used was methane, since a volatile dimethyl-zinc could form. In addition to methane, boron tetrachloride and hydrogen were also added for physical bombardment to break ZnO bonds and additional volatile reactions, respectively. After the etch, overhead and 45° SEM images were taken (shown in figure 4.2); while the images are encouraging, it is still not conclusive how much of the silicon dioxide mask has been etched or how much the GZO was undercut. After testing, we soon realized that this particular dry etch recipe also has problems; this is discussed in detail in chapter 6.

After the etch, the process for the gold windows is the same as before. We were now ready to test.

CHAPTER 5

EXPERIMENTAL SETUPS

In this chapter, diagrams for the experimental photoluminescence (PL) (figure 5.1) and time-resolved photoluminescence (TRPL) (figure 5.2) are provided with explanation:

The PL was used to determine the strength and emission wavelength of the sample at different temperatures. Because of non-uniformity in the sample, we could not necessarily claim that an enhancement in PL from the bow-ties is due to the plasmon-mediated photoluminescence (PMP). To more conclusively show that we are coupling to the nanostructure, a polarized PL was necessary; if we get the TM (HP) polarized PL to be noticeably stronger than the TE polarized PL on the bow-ties but not on the control sample, we could claim plasmonic coupling. As the temperature of the sample is increased, the emission wavelength red-shifts as a result of a smaller band gap. By varying temperature, we reasoned that there would be a change in coupling as the emission wavelength would eventually move away from the plasmonic resonance.

While the PL would give reasonable indication of whether or not the emitter is able to couple to the plasmonic structure, another way to determine the relative strength of coupling is to obtain the radiative lifetime. Ideally, we would expect shorter lifetimes when there is stronger coupling due to an enhancement of spontaneous emission rate from the Purcell effect. Hence, with the control sample, we would have a certain radiative lifetime; with a nanoantenna sample, due to the Purcell effect, the spontaneous emission rate would be enhanced and would therefore result in a shorter radiative lifetime.

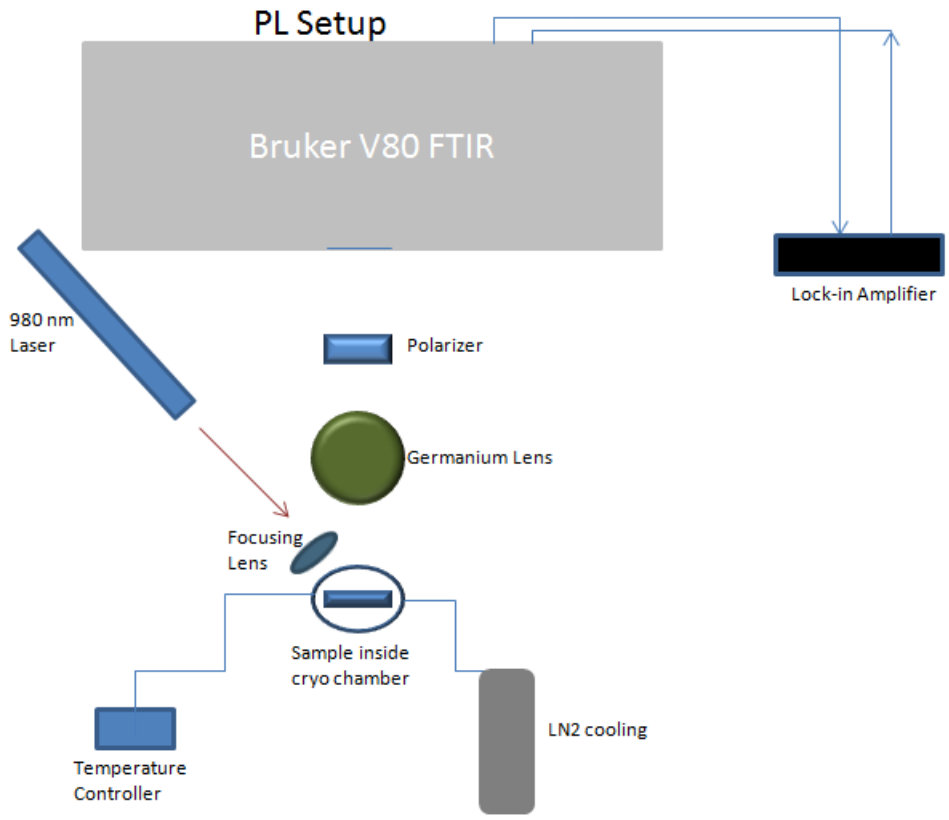

Figure 5.1: Diagram showing the PL setup. A 980 nm laser modulated at 10 kHz with approximately 70 mW of output power is focused and then hits the sample at an oblique angle. The surface of the sample emits and is collected and collimated by the germanium lens which also serves to absorb and block any reflected laser radiation. A polarizer is placed in front of the FTIR, which is used with a lock-in amplifier (LIA).

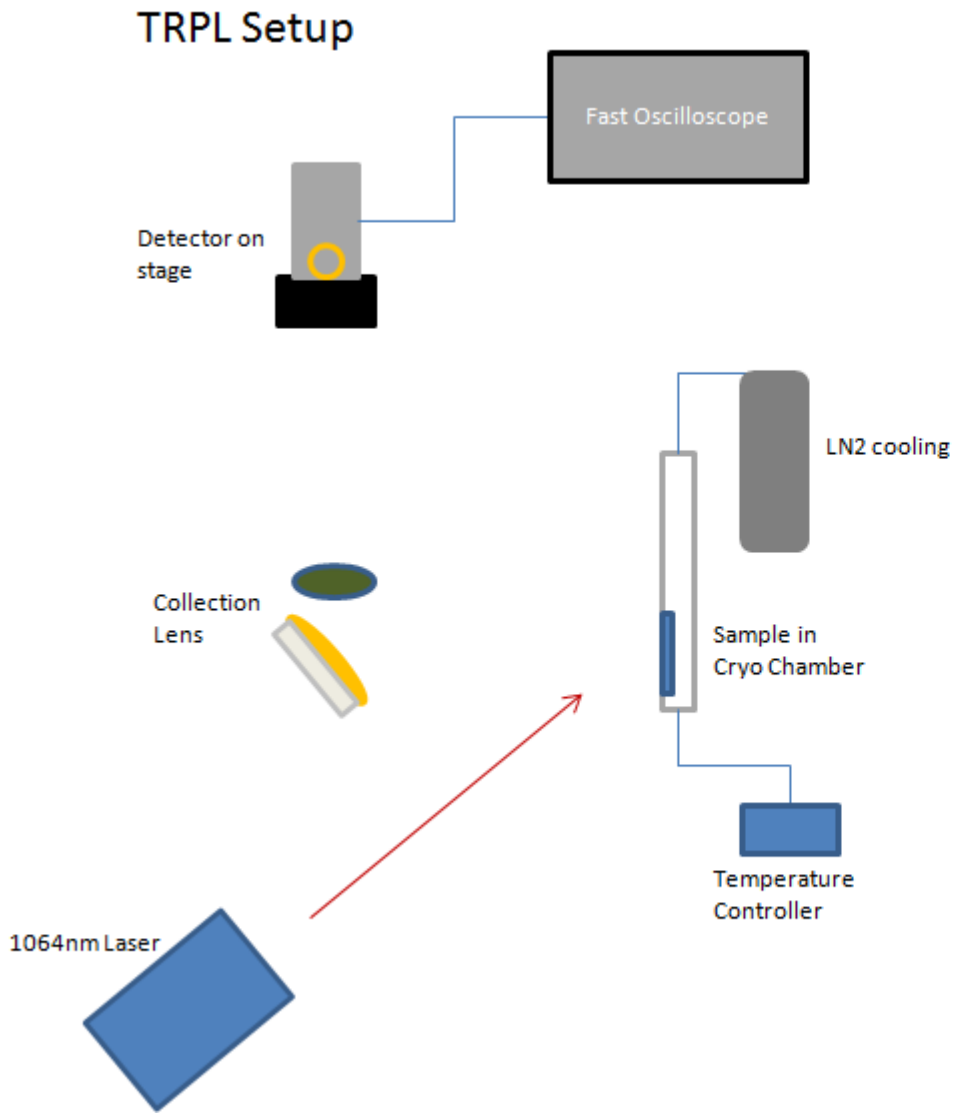

Figure 5.2: Diagram showing the TRPL setup. Radiation from a 12 kW peak power short pulsed 1064 nm laser modulated at 10 kHz is incident on a sample in a cryochamber at an oblique angle. Emission from the sample is focused using collecting lenses and then sent to a high-speed MCT IR detector. The signal from the detector is sent to an oscilloscope capable of resolving very short pulses. The time-resolved data is then analyzed to determine lifetimes.

CHAPTER 6

CURRENT RESULTS AND DISCUSSION

The polarized photoluminescence data for both the GZO on InAs and the GZO on $\lambda \approx 3.8$ μm emitter are shown and discussed in detail in this chapter.

6.1 Results from the GZO on InAs

Here, results from the initial lossy GZO on InAs are displayed. In chapter 3, theoretical reflection spectrum using RCWA was calculated. Both the calculated and experimental reflection using an IR-microscope with the FTIR are shown in figure 6.1.

Clearly, there is variation between the calculated and experimental spectra. The most likely cause of this discrepancy would be problems during fabrication; first of all, as explained in chapter 4, these initial bow-ties were etched with wet-etching. The undercutting from the wet-etching is unpredictable and hence does not guarantee the same shape used in the simulation. At the time, we thought that the higher reflection in the experimental spectrum is likely the result of incorrect GZO parameters used to simulate the nanostructure. Because of this, any GZO films deposited for the future nanoantennas were individually characterized using Hall-effect measurements to obtain a specific N and μ unique to that film deposit.

However, the photoluminescence data is the real test for whether we are able to couple to the plasmonic bow-tie nanoantennas. For this initial set of bow-ties fabricated on the InAs, we did not expect much enhancement of PL or difference in polarization as we likely undercut the GZO too much, which was thought to be too lossy anyway. Also, the plasmonic resonance was designed for $\lambda \approx 3.8$ μm. InAs emits at $\lambda \approx 3.0$ μm at 77 K, but the original idea was to increase the temperature, and by doing so, red-shift the emission wavelength; ideally, as the emission wavelength started to approach

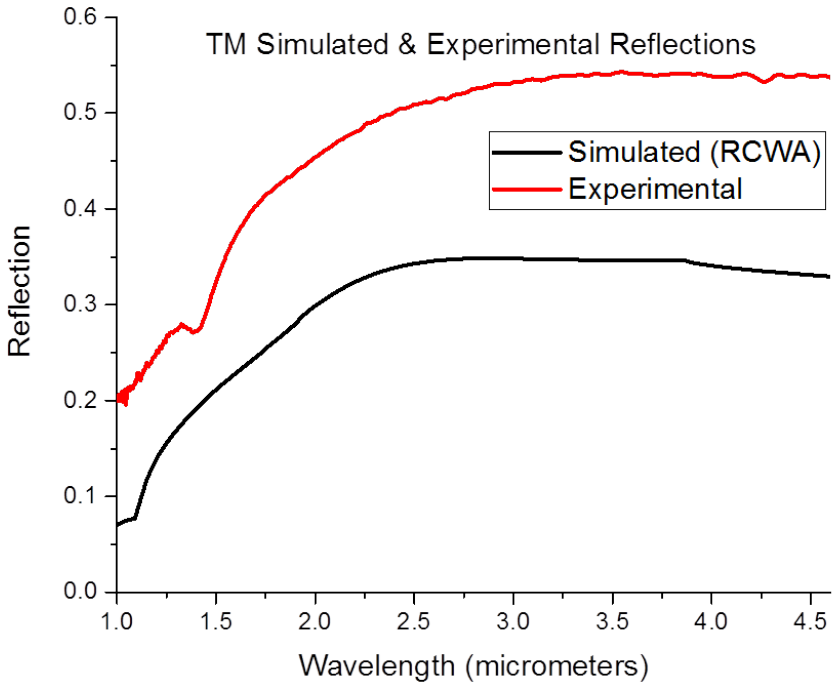

Figure 6.1: Experimental and theoretical reflection spectra

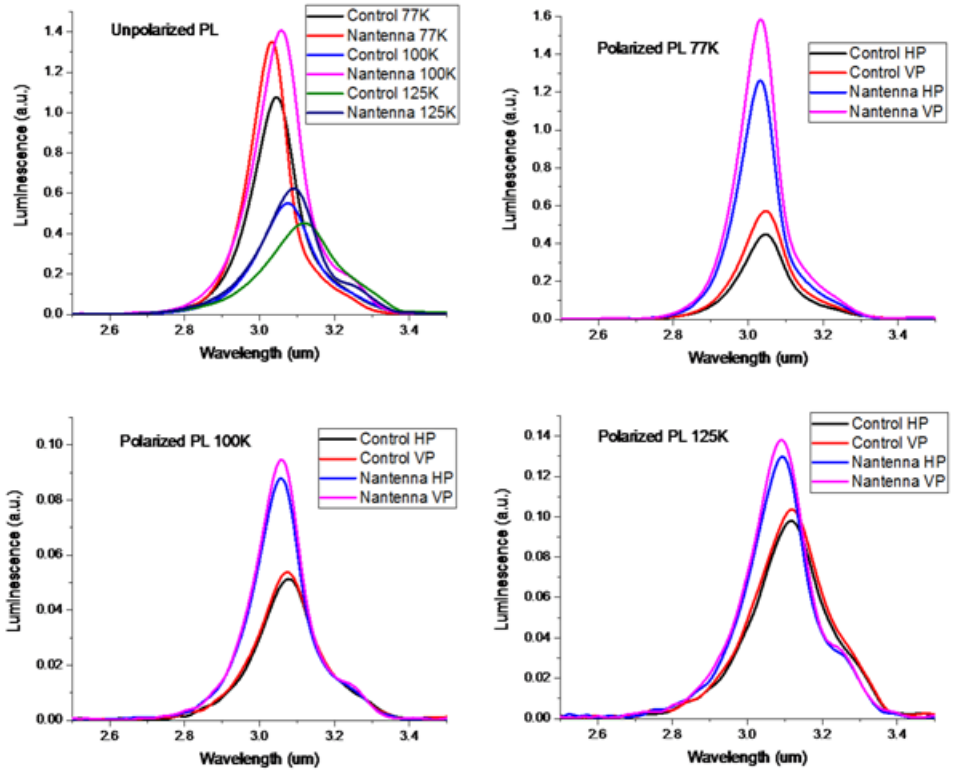

Figure 6.2: Polarized PL (UP - unpolarized, HP - horizontally, or TM, polarized, and VP - vertically, or TE, polarized) on the initial set of nanoantennas for three different temperatures.

the resonance wavelength, we expected to see a greater difference in PL between the bow-ties and the control sample as well as a greater difference between the TE and TM polarizations. However, since the InAs was not a very strong emitter, the data was too noisy for temperatures greater than 125 K. Figure 6.2 shows the results from the polarized PL at three different temperatures.

Even though the emission from the nanoantennas is stronger, because of the lack of difference between the polarizations on the nanoantenna sample relative to the control sample, it seems more likely that the enhancement of emission is due to possible scrapes in the gold surface of the sample near the 50 μm $\times$ 50 μm nanoantenna square window, resulting in a larger collection area from the nanoantenna window than the control sample window. To help control this in future nanoantenna samples, we decided to increase the size of the nanoantenna and control sample windows from 50 μm $\times$ 50 μm to 220

μm $\times$ 220 μm. By doing so, we could ensure that the laser beam spot would completely fall within the window so that any scrapes on the gold surface away from the testing window would fall outside the exciting laser beam's spot. From these results, it was clear that another set of bow-ties needed to be fabricated, preferably on a stronger emitter with an emission wavelength closer to the resonance wavelength at 3.8 μm.

6.2 Results from the GZO on $\lambda \approx 3.8\mu m$ Emitter

In figure 6.3, results from the polarized PL of the bow-tie nanoantennas at 77 K are shown. For this set of bow-tie nanoantennas, the sample was over-etched during the fabrication process. The gases used during dry etching were methane, boron tetrachloride, and hydrogen, as mentioned in chapter 4. However, because of the very large ICP power used, when the GZO was finished etching, the gases (primarily methane) started to etch and destroy the emitter material. Hence, there was undamaged emitter material only in regions under the bow-tie nanoantennas as the silicon dioxide mask pattern essentially protected both the GZO and the emitter material underneath. As a result, we were unable to see any emission at all from the control sample as the control sample did not have any silicon dioxide above it to protect it.

With the lack of a reliable control sample, we cannot claim enhancement from the bow-tie nanoantennas; in addition, it seems that the unpolarized PL intensity decreases with decreasing gap size, which is opposite to what is expected. However, as the gap size is decreased, we see that the sample emits more in the TM (HP) polarization than the TE polarization. While this is an expected result, we still require a reliable control sample to be able to draw any conclusions.

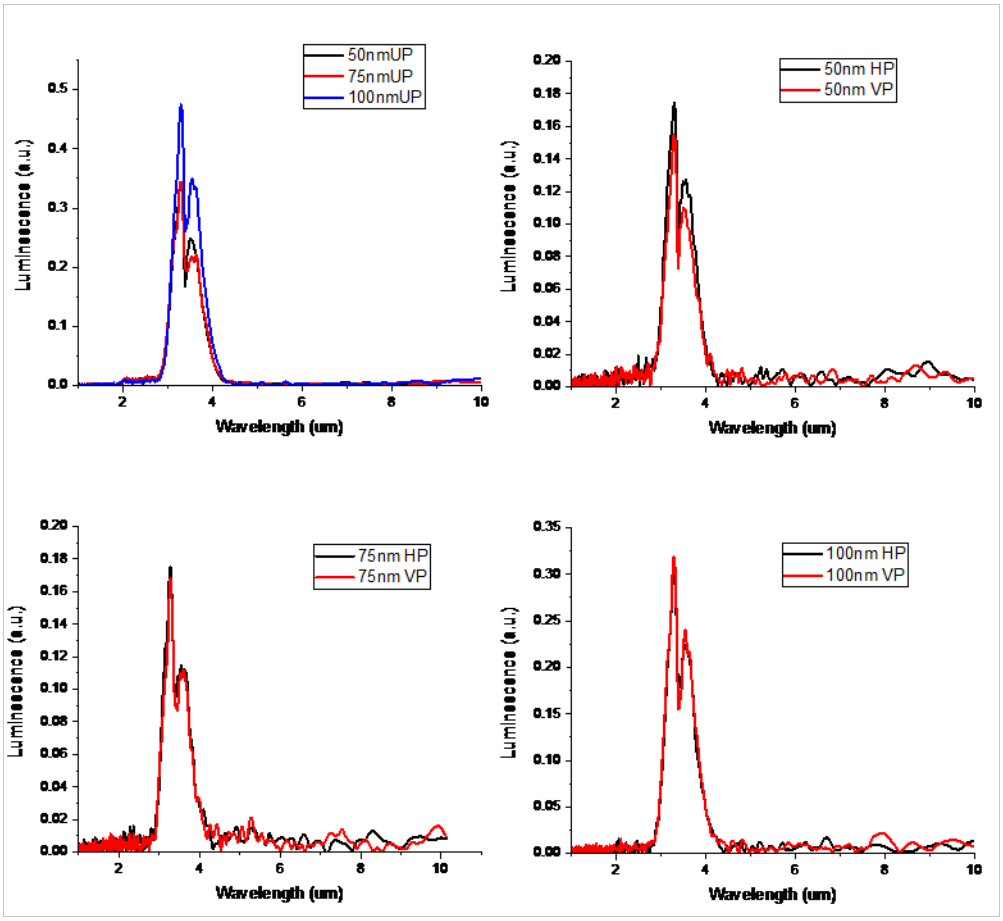

Figure 6.3: Polarized PL (UP - unpolarized, HP - horizontally, or TM, polarized, and VP - vertically, or TE, polarized) on the second emitter (with an ENZ layer) with nanoantennas made with less-lossy GZO film for three different bow-tie gap sizes at 77 K.

CHAPTER 7

FUTURE WORK AND CONCLUSION

Because the dry etch destroyed the second and most recent emitter, a different recipe must be used for etching. Since the methane was likely the gas responsible for etching away the emitter, we are going to try using only boron tetrachloride gas to etch the emitter; in addition, because this etch is slow compared to [14], it will be easier to avoid over-etching into the emitter.

Also, since the emitter from the last set of nanoantennas was leftover material from another project, it had an undesired ENZ layer on it as the ENZ does not aid the device in any way. For the set of nanoantennas currently being fabricated, the emitter is a quantum well emitter at $\lambda \approx 4.2$ μm in maximum emission wavelength made with four monolayers of InGaSb on InAs. The nanoantennas on this emitter have already been patterned with EBL and are now going to be dry-etched. Once fabricated, these devices will be tested with temperature-dependent polarized PL; if these results show enhancement in PL and favor TM polarization, then we will do a TRPL experiment to determine if the lifetimes are shorter for the nanoantennas than for the control sample. If all of these results are as expected, we can more conclusively claim that we are able to couple from our mid-IR emitter to the GZO plasmonic bow-tie nanoantennas and that in doing so, we have an enhancement in emission.

Overall, our results have laid the groundwork for further study of enhanced light-matter interactions due to designer plasmonic materials in the mid-IR. While plasmon-mediated photoluminescence has been studied with metallic nanoparticles in the visible wavelength region, it is a relatively novel and unexplored mechanism in the mid-IR. Though our preliminary results are in no way conclusive, some of the features mentioned in chapter 6 show promise for future nanoantenna samples. Hence, more time and research are needed to engineer practical devices in the mid-IR using designer plasmonic materials.

REFERENCES

[1] F. K. Tittel, D. Richter, and A. Fried, "Mid-infrared laser applications in spectroscopy," in *Solid-State Mid-Infrared Laser Sources*. Springer, 2003, pp. 458–529.

[2] M. Razeghi, A. Evans, J. Nguyen, Y. Bai, S. Slivken, S. Darvish, and K. Mi, "High-power mid-and far-wavelength infrared lasers for free space communication," in *Microtechnologies for the New Millennium*. International Society for Optics and Photonics, 2007, pp. 65 931V–65 931V.

[3] C. Pidgeon, C. Ciesla, and B. Murdin, "Suppression of non-radiative processes in semiconductor mid-infrared emitters and detectors," *Progress in Quantum Electronics*, vol. 21, no. 5, pp. 361–419, 1997.

[4] A. Stiff, S. Krishna, P. Bhattacharya, and S. Kennerly, "High-detectivity, normal-incidence, mid-infrared InAs/GaAs quantum-dot detector operating at 150 k," *Applied Physics Letters*, vol. 79, no. 3, pp. 421–423, 2001.

[5] S. A. Maier, *Plasmonics: Fundamentals and Applications*. Springer Science & Business Media, 2007.

[6] T. W. Ebbesen, H. J. Lezec, H. Ghaemi, T. Thio, and P. Wolff, "Extraordinary optical transmission through sub-wavelength hole arrays," *Nature*, vol. 391, no. 6668, pp. 667–669, 1998.

[7] S. L. Chuang, *Physics of Photonic Devices*. John Wiley & Sons, 2012.

[8] P. Peumans, A. Yakimov, and S. R. Forrest, "Small molecular weight organic thin-film photodetectors and solar cells," *Journal of Applied Physics*, vol. 93, no. 7, pp. 3693–3723, 2003.

[9] C. Ropers, C. Neacsu, T. Elsaesser, M. Albrecht, M. Raschke, and C. Lienau, "Grating-coupling of surface plasmons onto metallic tips: a nanoconfined light source," *Nano Letters*, vol. 7, no. 9, pp. 2784–2788, 2007.

[10] D. Look and K. Leedy, "ZnO plasmonics for telecommunications," *Applied Physics Letters*, vol. 102, no. 18, p. 182107, 2013.

[11] K. R. Williams, K. Gupta, and M. Wasilik, "Etch rates for micromachining processing-Part II," *Microelectromechanical Systems, Journal of*, vol. 12, no. 6, pp. 761–778, 2003.

[12] H.-K. Kim, J. Bae, T. Kim, K. Kim, T. Y. Seong, I. Adesida et al., "Inductively coupled plasma reactive ion etching of ZnO using BCl_3-based plasmas," *Journal of Vacuum Sscience and Technology*, vol. 21, no. 4, pp. 1273–1277, 2003.

[13] J. Park, H. Park, Y. Hahn, G.-C. Yi, and A. Yoshikawa, "Dry etching of ZnO films and plasma-induced damage to optical properties," *Journal of Vacuum Science & Technology B*, vol. 21, no. 2, pp. 800–803, 2003.

[14] J.-W. Bae, C.-H. Jeong, H.-K. Kim, K.-K. Kim, N.-G. Cho, T.-Y. Seong, S.-J. Park, I. Adesida, and G.-Y. Yeom, "High-rate dry etching of ZnO in $BCl_3/CH_4/H_2$ plasmas," *Japanese Journal of Applied Physics*, vol. 42, no. 5B, p. L535, 2003.